Manchester Metropolitan University

e-space

Manchester Metropolitan University's Research Repository

Please cite the Published Version

Soper, David, Baker, Chris and Sterling, Mark (2015) An experimental investigation to assess the influence of container loading configuration on the effects of a crosswind on a container freight train. Journal of Wind Engineering and Industrial Aerodynamics, 145. pp. 304-317. ISSN 0167-6105

DOI: https://doi.org/10.1016/j.jweia.2015.03.002

Publisher: Elsevier BV

Version: Accepted Version

Downloaded from: https://e-space.mmu.ac.uk/634424/

Usage rights: CC BY-NC-ND Creative Commons: Attribution-Noncommercial-No Derivative Works 4.0

Additional Information: © 2015. This manuscript version is made available under the CC-BY-NC-ND 4.0 license https://creativecommons.org/licenses/by-nc-nd/4.0/

Enquiries:
If you have questions about this document, contact openresearch@mmu.ac.uk. Please include the URL of the record in e-space. If you believe that your, or a third party's rights have been compromised through this document please see our Take Down policy (available from https://www.mmu.ac.uk/library/using-the-library/policies-and-guidelines)

An experimental investigation to assess the influence of container loading configuration on the effects of a crosswind on a container freight train

David Soper, Chris Baker, Mark Sterling

Birmingham Centre for Railway Research and Education, School of Civil Engineering, University of Birmingham, UK

Corresponding author:

David Soper, Birmingham Centre for Railway Research and Education, School of Civil Engineering, University of Birmingham, Edgbaston, Birmingham, B15 2TT, UK

Email: d.soper@bham.ac.uk

Abstract

Relative crosswinds when coupled with transient aerodynamic effects associated with freight trains can have large velocity magnitudes, potentially affecting the stability of not only the train but also containers loaded onto the train. This paper describes a series of moving model crosswind experiments conducted at the University of Birmingham's TRAIN rig facility using a Class 66 hauled container freight train fitted with an on-board surface pressure monitoring system. In the paper the term 'freight train' refers to a series of flatbed wagons loaded with ISO standard shipping containers hauled by a Class 66 locomotive. By altering the container loading efficiency it was possible to develop an understanding of influencing factors on forces subjected to a loaded container. Surface pressure coefficient data has been recorded at a yaw angle of 30°; and were compared with data corresponding to a typical passenger train. In general, similar magnitudes of pressure coefficients have been observed. However, areas associated with large flow separation exhibited greater magnitudes than previously observed. The pressure coefficient magnitudes measured on the container surface exhibited clear dependence on container loading configuration. A series of pressure gradients were observed for different container faces, relating to the crosswind flow over the container and a series of vortices formed at unshielded container edges. It was possible to calculate the overall mean aerodynamic load coefficients as a discrete integral of forces acting on each pressure tap area. Larger magnitudes for aerodynamic load coefficients were observed as container loading efficiency was reduced and the space size in front of the measuring container increased. Overall the results from this paper offer for the first time a definitive study on the influence of container loading configuration on the characteristics of aerodynamic loads subjected to a container freight train travelling through a crosswind.

Keywords: Aerodynamics, crosswind, freight train, slipstream, pressure coefficient, aerodynamic load coefficient, experimental study, model-scale.

Notation

A_{ij}	discretised container surface areas associated with pressure tap ij
A_{ref}	nominal side area of container (m^2)
C_P	coefficient of pressure
C_ζ	aerodynamic load coefficients for $\zeta = Y, Z$ and $M_{X,lee}$
E_η	uncertainties for $\eta = BIAS, RAND, TOT$ and $LOAD$
ENS	ensemble averaged
F_ξ	aerodynamic forces for $\xi = Y, Z$ (N)
$M_{X,lee}$	aerodynamic moment about the leeside container base edge (Nm)
H_{ref}	nominal container height (m)
I_ξ	on set crosswind turbulence intensities for $\xi = u_{cwg}, v_{cwg}$ and w_{cwg} (%)
$L_{cwg_{S_N}}$	portion of crosswind test section associated with spanwise position S_N (m)
N	number of positions tested in crosswind generator flow characterisation
P_{ij}	instantaneous surface pressure at tap ij (Pa)
P_{ST}	on set crosswind static pressure (Pa)
R	gas constant (J/kg K)
S_N	spanwise position
SW	spanwise average
V_{rel}	relative crosswind velocity (m/s)
V_{train}	train speed (m/s)
X	longitudinal axis defined in the direction of train travel measured from the crosswind generator entrance
Y	lateral axis defined in the horizontal plane perpendicular to the direction of train travel measured from the centre of track
Z	vertical axis measured from the top of the rail
Z_{ref}	crosswind reference height (m)

d_{ij}	vectors perpendicular to the container base leeward edge, directed from each pressure tap
i	pressure taps number on loop j
j	loop of pressure taps
k	pressure transducer associated with pressure tap ij
n_{ij}	normal unit vectors associated with discretised areas A_{ij}
r	number of independent runs undertaken to create the ensemble average
t	time (s)
u_{cwg}	on set crosswind streamwise longitudinal component of velocity (m/s)
v_{cwg}	on set crosswind lateral component of velocity (m/s)
w_{cwg}	on set crosswind vertical component of velocity (m/s)
ρ	density of air (kg/m^3)
θ	yaw angle (°)
$*$	corrected to account for streamwise gradients in crosswind flow
∂b_k	instrumentation uncertainties

1. Introduction

Transient air flows created by vehicle movement when coupled with outside effects such as crosswinds can have serious consequences. On the 1st March 2008, in two separate incidents, a total of seven containers were blown from flatbed freight wagons travelling along the West Coast Mainline, UK (figure 1). The effect of vehicle induced slipstream velocities coupled with strong gusty crosswind conditions and a failure of equipment was found to be the incidents cause (RAIB, 2009). In America and Australia a number of similar incidents have occurred with double stack container freight trains travelling in strong crosswind conditions or through exposed routes (ATSB, 2008). Although such incidents are rare these examples highlight the importance of understanding air flows around freight trains. Knowledge of aerodynamic load coefficient magnitudes is therefore important in the authorisation of increased train speeds and development of new trains (Baker et al., 2013).

Figure 1: Detached containers blown from flatbed freight wagons travelling along the West Coast Mainline, UK, on the 1st March 2008 (RAIB, 2009).

The UK government has set aims to double the volume of rail freight cargo on the UK rail network by 2030 (DFT, 2007). Efficiency studies into increased volumes of freight trains recommend developing faster and longer trains (Woodburn, 2008). This however has implications on the magnitude and incident angle of relative crosswinds. The effect of increasing train speeds increases the magnitude of slipstream velocities and transient aerodynamic effects created by vehicle movement (Soper et al., 2014). When coupled with a crosswind the magnitude of these effects are increased and can potentially affect the relative stability of loaded containers.

Transient air flows created by vehicle movement when coupled with naturally turbulent crosswinds can create a series of steady and unsteady aerodynamic forces and moments (Dorigatti, 2013; Dorigatti et al., 2014). These aerodynamic loads can potentially induce significant changes to vehicle dynamic behaviour, possibly compromising stability. A train will overturn when the contribution of the aerodynamic rolling moment about the leeward rail, generated by a crosswind, is large enough to overcome the restoring moment associated with the train weight (Gawthorpe, 1994; RSSB, 2009). The investigation of crosswind effects on rail vehicles has been the subject of a number of studies concerned with the inherent risks of vehicle overturning and track instability (Gawthorpe, 1994; Andersson et al., 2004; Alam and Watkins, 2007a,b; Baker and Sterling, 2009). Research has predominantly focused on passenger trains due to the possible impact of loss of life if a vehicle were to overturn (Raghunathan et al., 2002). However, in light of the recent container freight crosswind incidents there have been a series of investigative national safety reports commissioned and published (RAIB, 2009; ATSB, 2008; TSI, 2008), leading to fundamental research projects focused on freight in crosswind conditions (Alam and Watkins, 2007a; Hemida and Baker, 2010; RSSB, 2012).

This paper will present and analyse the results of a series of experiments to assess the influence of container loading efficiency on aerodynamic load magnitudes measured on a container mounted onto a freight train. Moving model-scale experiments were undertaken using the crosswind generator at the University of Birmingham's TRAIN (TRansient Aerodynamic INvestigation) rig in Derby. The experiment facility and crosswind generator are described in section 2.1. Section 2.2 introduces the TRAIN rig freight model and the adaptations made to conduct the crosswind experiments. The adopted coordinate system, experiment methodology and trackside instrumentation are discussed in section 2.3. Section 2.4 introduces the method of data processing and section 2.5 presents an estimation of the error associated with the results. The experimental results and analysis are presented in section 3 for coefficient of pressure (section 3.1), and aerodynamic load coefficients (section 3.2). Finally, section 4 presents conclusions drawn from this study. Full details of the work presented in this paper can be found in the first author's doctoral study (Soper, 2014).

2. Experimental methodology

2.1 TRAIN rig and crosswind generator

The TRAIN rig is a purpose built testing facility for examining the transient aerodynamics of moving vehicles (Baker et al., 2001). It consists of three 150 m long tracks along which reduced scale vehicles can be propelled at speeds up to 75 m/s. The TRAIN rig offers the possibility to measure slipstream velocities, static pressure pulses and pressures acting on the train or trackside structures in a 12 m long open air test section (Baker et al., 2014). A 27 m long tunnel is also installed for the measurement of vehicle aerodynamics in tunnel confines. The advantage of using a moving model rig over a typical stationary wind tunnel is the ability to correctly simulate relative motion between the vehicle and the ground/structures or crosswind simulation.

The TRAIN rig incorporates a specifically designed crosswind generator as shown in figure 2. The crosswind generator consists of a series of 16 axial flow fans (Ziehl-Abegg, 2014) arranged in two rows of eight units positioned at the trackside. The fans are attached to a steel supporting structure built into an enclosed unit to ensure flow is entrained within a 6.35 m test section, through which the TRAIN rig tracks pass. Due to constraints associated with the TRAIN rig location, the crosswind generator is constructed completely within the building envelope. The fans operate as an open circuit design by which air is sucked through an enclosed duct, generating flow directed perpendicular to the tracks. Exhausted air is recirculated inside the building. The crosswind generator test section extends 1.685 m in the mean flow direction, 1m in height above the top of the rail, over 6.35 m of track. For this study a flat ground simulation is modelled, such that the ground plane is level with the top of rail. The crosswind generator can also be used for static model wind tunnel tests with the implementation of a turntable. A detailed discussion of the crosswind generator development and a comparison of static and moving model experiments for a Class 390 high speed passenger train can be found in Dorigatti (2013) and Dorigatti et al. (2014).

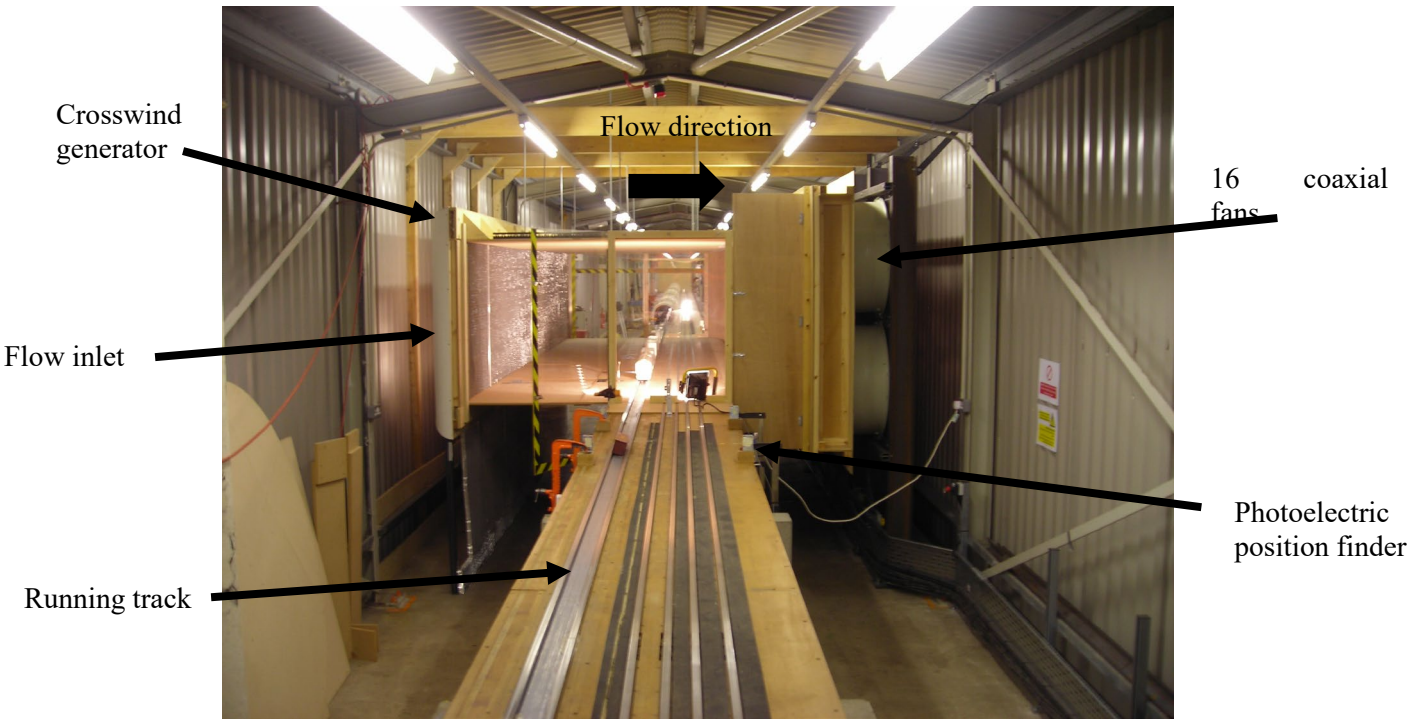

a) TRAIN rig crosswind generator

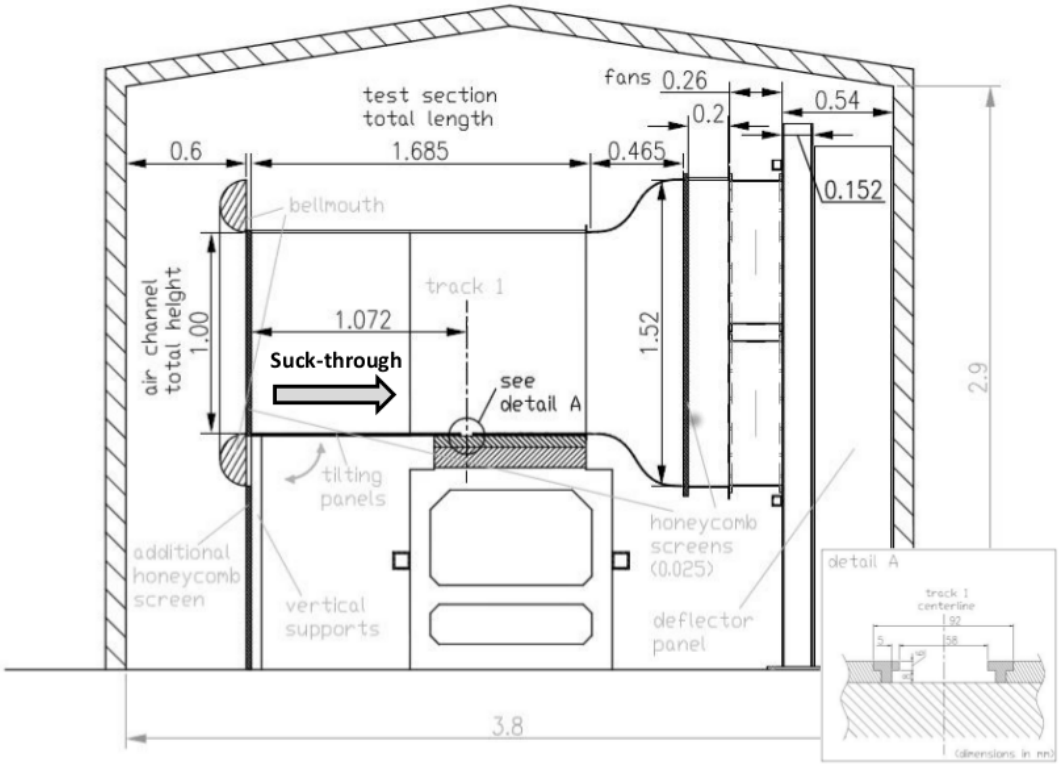

b) TRAIN rig crosswind generator schematic (along track view)

Figure 2: The TRAIN rig crosswind generator. The 16 axial flows fans are situated to the right of the photograph, with simulated crosswind flows from the left to the right in figure 2a).

An in-depth flow characterisation of the crosswind generator, using Turbulent Flow Instrumentation Series 100 Cobra probes (TFI, 2011) to create horizontal and vertical wind profiles, was carried out by Dorigatti (2013). The Cobra probe accuracies for velocities and static pressure are ±0.3 m/s and ±5 Pa respectively. A horizontal wind profile was created by measuring sixty four spanwise positions S_N, distributed parallel to the track at a distance 0.2 m upstream of the running track at a height of $Z_{ref} =$ 0.12 m. The height $Z_{ref} = 0.12$ m, equivalent to 3 m at full-scale with respect to the modelling scale of 1/25th, is adopted as a reference height for this study in line with previous studies (Baker and Sterling, 2009; Dorigatti, 2013). Figure 3 illustrates the horizontal mean (time averaged) wind profile for streamwise $\overline{u_{cwg}}$, lateral $\overline{v_{cwg}}$, and vertical $\overline{w_{cwg}}$ velocities and the mean static pressure $\overline{P_{ST}}$, as well as turbulence intensities, with respect to the atmospheric pressure.

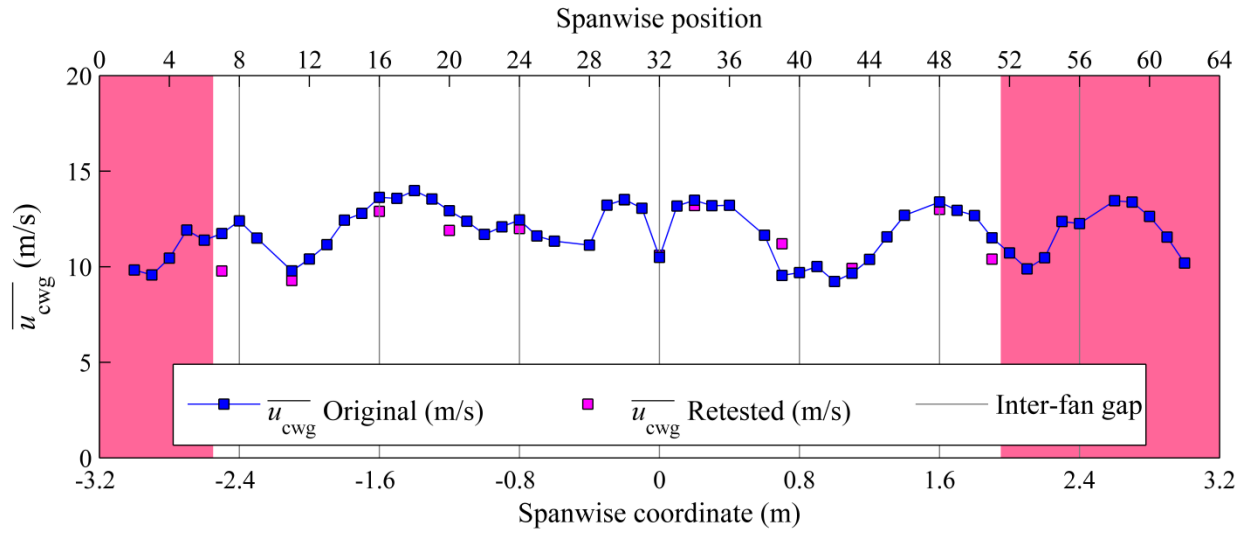

a) Mean velocity $\overline{u_{cwg}}$

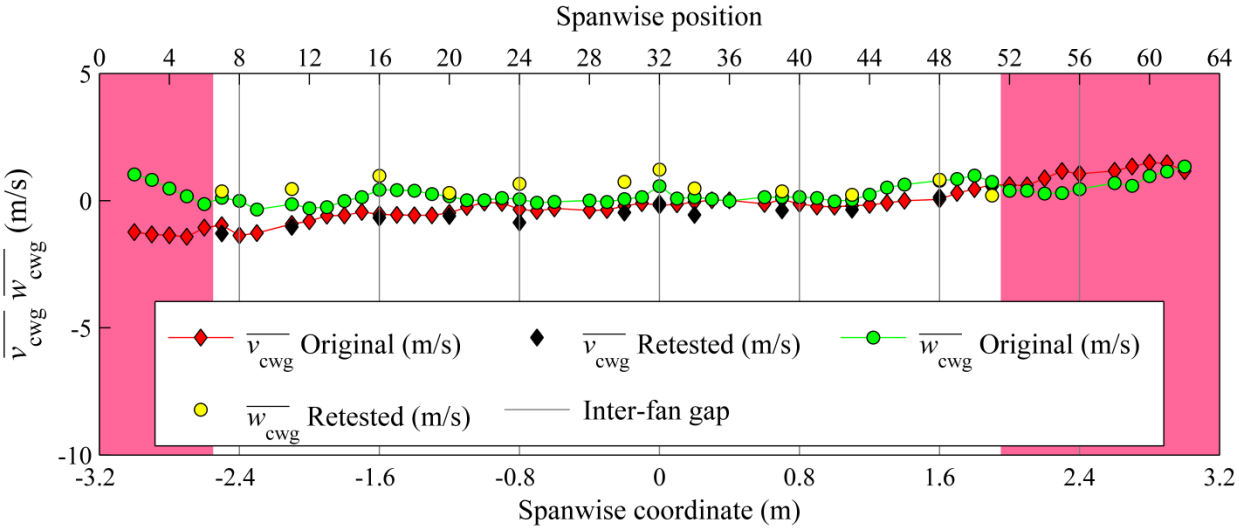

b) Mean velocities $\overline{v_{cwg}}$ and $\overline{w_{cwg}}$

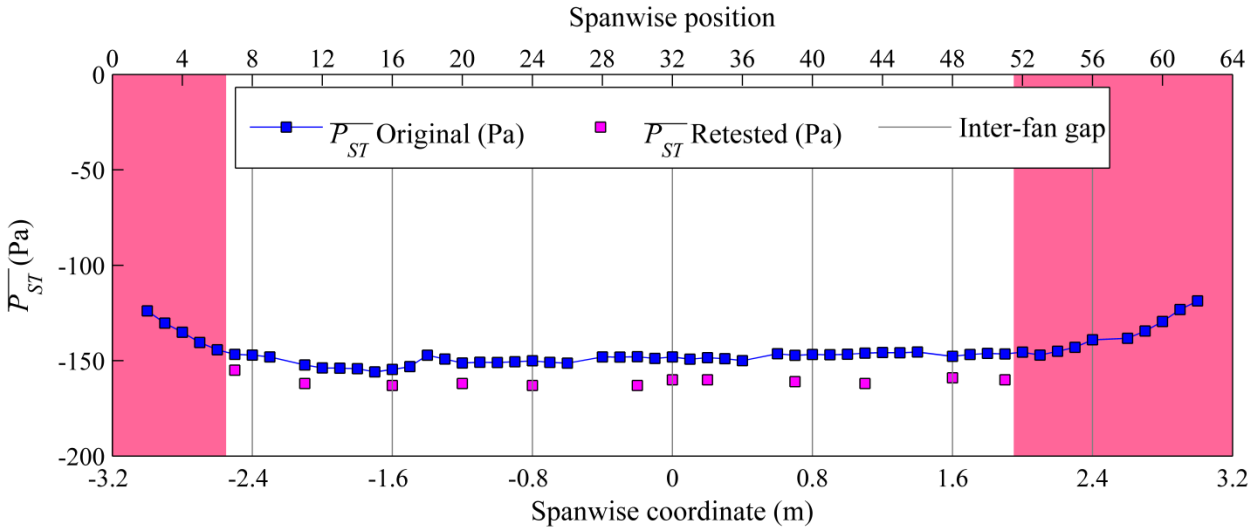

c) Mean static pressure $\overline{P_{ST}}$

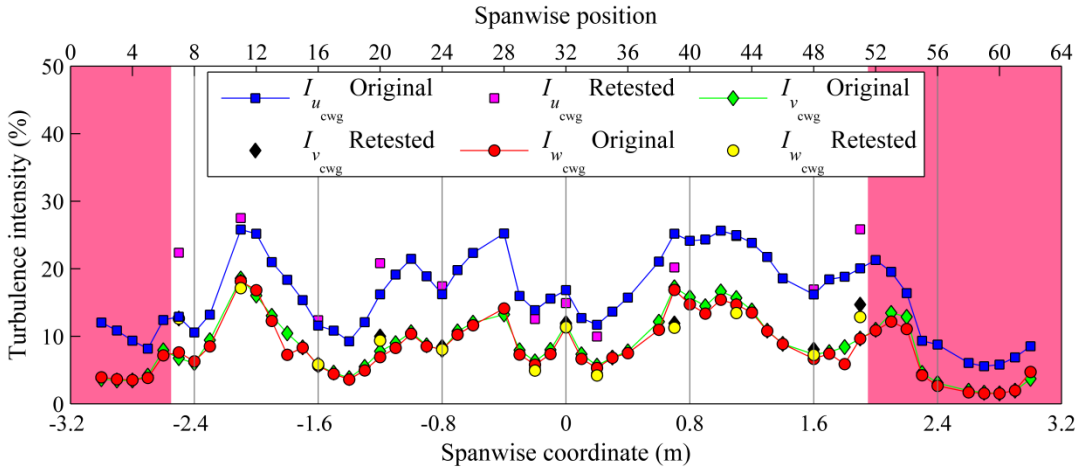

d) Mean turbulence intensities

Figure 3: A comparison of horizontal wind profiles for a) the streamwise mean velocity $\overline{u_{cwg}}$, b) the lateral $\overline{v_{cwg}}$ and vertical $\overline{w_{cwg}}$ mean velocities, c) mean static pressure $\overline{P_{ST}}$ and d) turbulence intensities for the Dorigatti (2013) crosswind generator flow characterisation and a series of retested points. Vertical grey lines indicate the inter-fan gap. Shaded red areas indicate sections of the crosswind generator affected by the model entrance portals, subsequently left out from this study.

The flow characterisation exhibited relatively consistent spanwise uniformity for the mean streamwise component of velocity $\overline{u_{cwg}}$ (Dorigatti, 2013). Lateral mean velocities $\overline{v_{cwg}}$ show negative then positive values across the horizontal profile, consistent with air not only drawn in through the inlet section but also sucked through the model entrance portals at each side of the crosswind generator. Dorigatti et al. (2014) concluded that measurements should be disregarded for the initial 1.27 m and final 0.64 m of the crosswind generator, measured in the direction of model travel. The entrance portal influence is also observed for static pressure $\overline{P_{ST}}$, which exhibits relatively stable values across the central portion of the crosswind generator but large differences in the areas disregarded near the model vehicle entrance portals. Limited spanwise uniformity was found for turbulence intensities, related to a series of amplifications associated with $\overline{u_{cwg}}$ and the relative position in relation to the fans. The flow characterisation allowed spanwise averages to be calculated, shown in table 1 (Dorigatti, 2013).

Spanwise average	u_{cwg} (m/s)	v_{cwg} (m/s)	w_{cwg} (m/s)	P_{ST} (Pa)	$I_{u_{cwg}}$ (%)	$I_{v_{cwg}}$ (%)	$I_{w_{cwg}}$ (%)
Central span (-2.55 m to 1.95 m)	12	-0.3	0.2	-150	18	10	9

Table 1: Spanwise averages for the horizontal wind profile calculated from the Dorigatti (2013) crosswind flow characterisation at reference height $Z_{ref} = 0.12$ m.

2.2 TRAIN rig model freight train

A 1/25th scale moving model freight train was designed to simulate container loading configurations seen at full-scale. Unlike focusing on a specific high speed passenger train the term 'freight train' applies to many different train types (e.g. containers, tankers, mineral wagons etc.). For this study the term ‘freight train’ refers to a series of FEA type B flatbed wagons loaded with International Shipping Organisation (ISO) standard shipping containers hauled by a Class 66 locomotive. Container freight is one of the largest sectors of freight transported in the UK and the choice for this study offers relative ease for modelling purposes. An existing Class 66 model was modified to include a long flat plate to simulate four FEA type B flatbed wagons, with bogies modelled using balsa wood (figure 4). The model is mounted on a specially designed chassis and trailing wheel system, designed to distribute the model weight evenly, thereby providing stability and a structure by which to fire/brake the model. The chassis and trailing wheel system allows the train to move along the track in a longitudinal direction but negates lateral and vertical motion. Figures 5 gives dimensions (expressed in terms of a full-scale equivalent) for the Class 66 and a twin set of FEA type B wagons respectively. Further information on the development of the TRAIN rig freight train is discussed in detail by Soper et al. (2014).

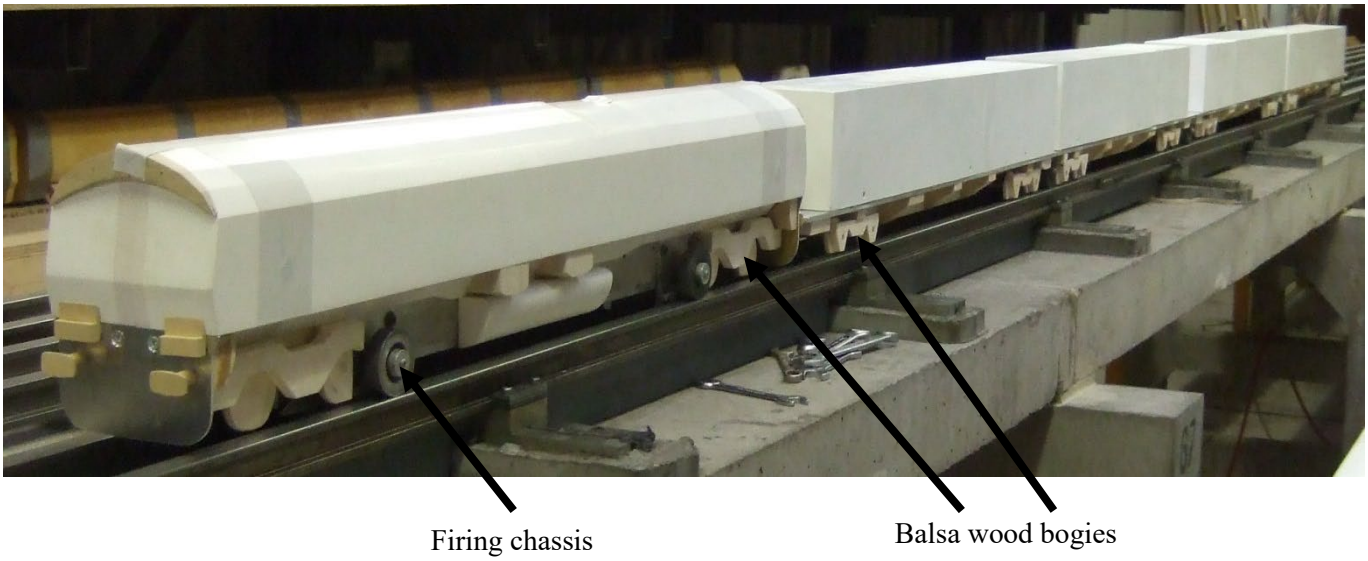

Figure 4: TRAIN rig model freight train. The train consists of a Class 66 locomotive and a four FEA type B wagons. The container loading configuration shown in the figure is consist 1 with 100% loading efficiency.

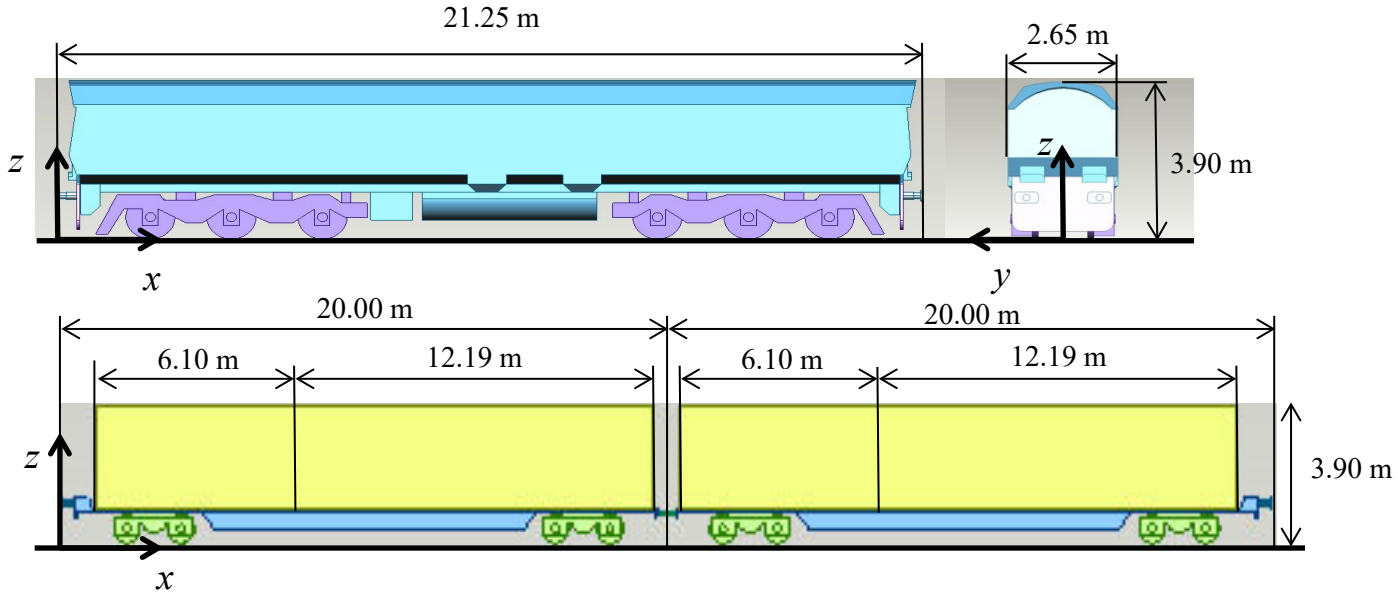

Figure 5: Dimensions for the Class 66 locomotive and a FEA type B wagon twin set. All dimensions are given in terms of a full-scale train.

Twelve scale 6.10 m containers, and eight 12.19 m containers were arranged in various configurations to represent a cross section of different container loading efficiencies as shown in figure 6. Container surfaces were simplified by neglecting a series of corrugations; this is consistent with the approach adopted in previous research by Alam and Watkins (2007a) and Hemdia and Baker (2010) with satisfactory results.

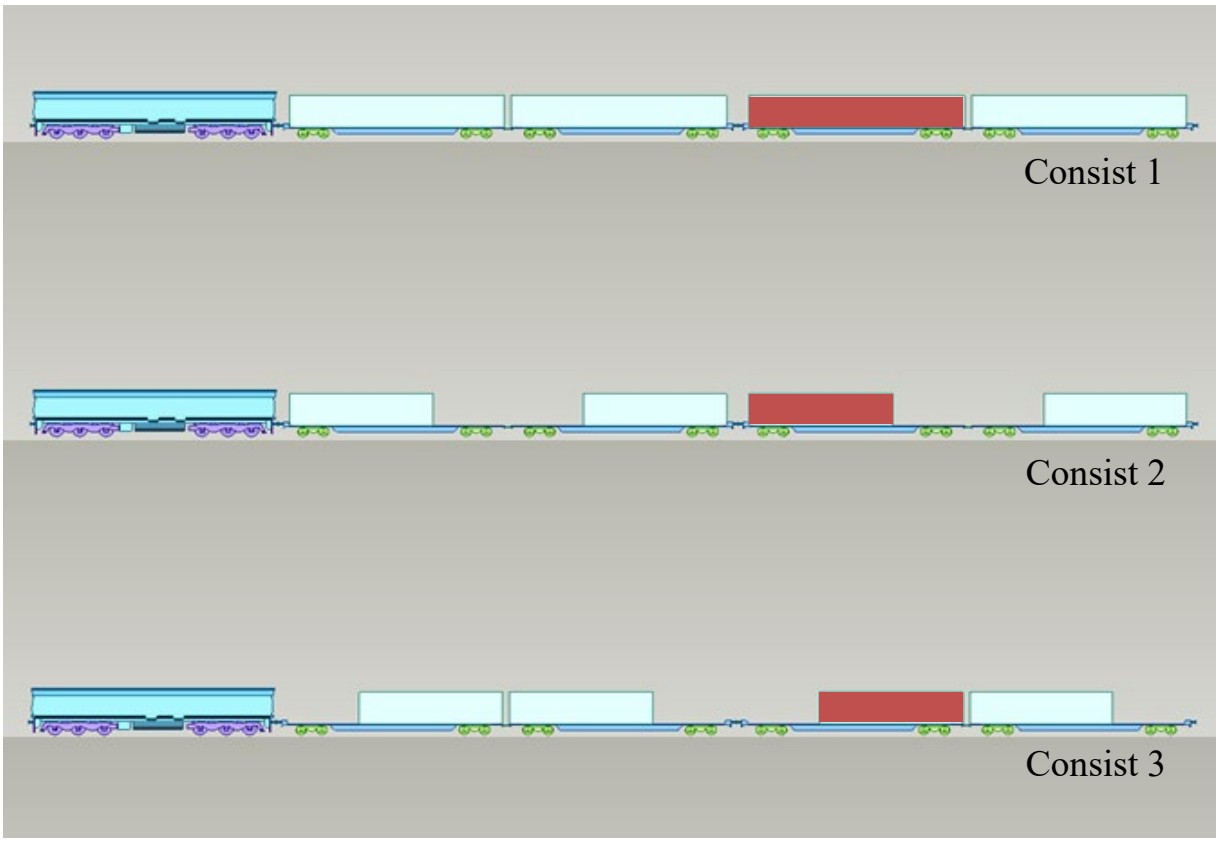

Figure 6: The container loading configurations used in this paper. Consists 1, 2 and 3 have 100%, 66% loading efficiencies respectively. The model train with consist 1 is also shown in figure 4. The measuring container is highlighted red for each consist.

A novel on-board pressure monitoring system with a stand-alone data logger was built into a scale 12.19 m x 2.44 m x 2.59 m container. The system consists of a stand-alone data logger powered by a rechargeable battery, connected via three-core shielded cables to fifteen HCLA12X5PB miniaturised differential pressure transducers (Sensortechnics, 2013) and a light detector [Vishay Intertechnology Inc., VISHAY-TEPT5600]. The piezoresistive miniaturised amplified differential low pressure sensors have a ±1250 Pa range and an analogue signal range 0-5Volts, with an accuracy of ±5 Pa. The pressure transducer measuring ports were connected via silicon tubing to metal tubing adapters glued into the container side walls, acting as pressure taps. The pressure transducer reference ports were connected via silicon tubing to a manifold which was in turn connected to a sealed reservoir, acting as an on-board reference pressure system. As the system is sealed it was susceptible to drift created, for example, by variations in ambient temperature. Typical values of drift recorded during the experiments were less than ±2 Pa, below the estimated instrumentation accuracy. To negate any possible effects of drift in the sealed reservoir, a vent was fitted into the system which could be opened after every run. The purpose built stand-alone data logger has a 16-bit resolution and is capable of monitoring 16 channels at a maximum sampling rate of 4000 Hz. To ensure usability of the logger, an on/off switch and coaxial socket, to connect the data logger to a laptop, were mounted to the container walls.

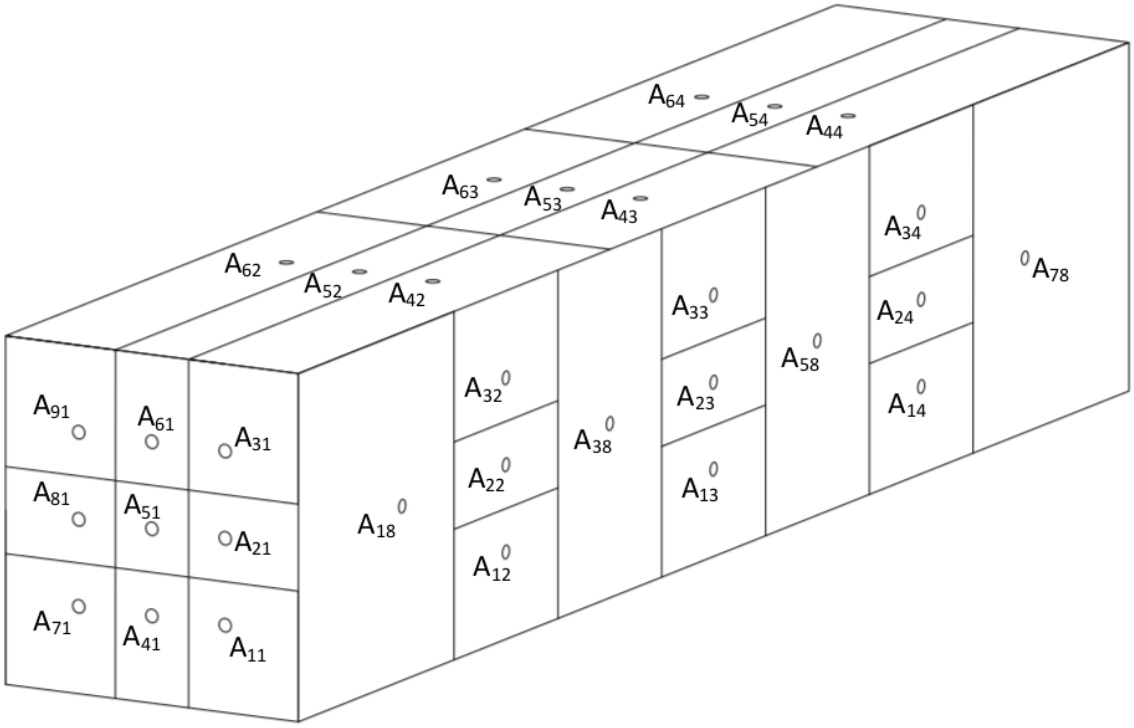

Figure 7: Pressure tap positions and associated discretised areas to each tapping point for the 12.19 m measuring container. An index system is used to identify pressure taps such that ***ij*** is defined where ***j*** is the tapping loop and ***i*** is the associated tap on that loop. The container is rotated about the third wagon to create the loading configurations seen in figure 6.

An array of nine pressure taps were positioned at the container end face and loops of nine taps were positioned at 25% and 50% of the container length, shown in figure 7. In addition to these loops, pressure taps were placed at container mid-height at 12.5% and 32.5% of container length on each side, creating a ring of pressure taps at mid-height around the container. It should be noted that no pressure taps were placed in the container base as a result of the flexible fixing mechanism used to connect the container to the flatbed wagon. The measuring container is detachable from the wagon, enabling measurements to be made at different positions along the train.

Soper et al. (2014) presented a discussion of freight train model length in relation to slipstream development, and discovered that for container loading configurations with a loading efficiency below 50% a train of more than five wagons was needed to observe the transition from boundary layer growth to boundary layer equilibrium. However, for higher loading efficiencies boundary layer equilibrium could be observed for a four wagon train. The results presented in this paper are for container loading efficiencies greater than 50%, therefore a four wagon freight train was used. Three loading configurations were tested with loading efficiencies of 100% and 66% (figure 6). Consist 3

was chosen to analyse the influence of individual container positioning in relation to consist 2. Previous container freight wind tunnel studies found 1.5 wagons before and 0.5 wagons following the measuring wagon were required to observe the wagon consist influence (Saunders et al., 1993). Therefore, the third wagon behind the Class 66 locomotive was chosen as the measuring wagon onto which the measuring container was mounted. As the measuring container is detachable it was possible to rotate the container by 180 degrees, thus creating in effect five loops with a total of 53 pressure taps for consist 2 and 3 and seven loops with a total of 75 pressure taps for consist 1. As the data logger only has sixteen channels the number of pressure transducers recorded simultaneously is limited; therefore, for each consist the pressure tapping loops were divided into a series of tapping setups. For consist 1 the 75 pressure taps were divided into six setups, and similarly for consists 2 and 3 the 53 pressure taps were divided into four setups.

A number of simplifications were made to conduct the crosswind experiments at model-scale. Detailed components such as bogies were geometrically simplified and the experiment was conducted as an open track with no ballast shoulder modelled. Simplifications of a similar manner have been previously adopted for model-scale studies of high speed passenger trains (Baker et al., 2001; Dorigatti et al., 2014). Throughout this study a train speed V_{train} = 20.8±0.5 m/s (45±1 mph) was chosen to create a yaw angle to the onset wind of 30°. However, a model vehicle speed decay of ~1.1 m/s was observed through the crosswind generator, caused by friction and aerodynamic drag. By assuming a linear decrease in train speed through the crosswind generator, the train speed required as the train enters the crosswind test section was 21.2±0.5 m/s, ensuring a yaw angle of 30° ± 1°. The corresponding Reynolds number for these experiments is 2.5×10^5 based on the relative crosswind velocity V_{rel} and the Class 66 height (156 mm at 1/25th scale).

2.3 Coordinate system and trackside measuring instrumentation

The coordinate system adopted is defined in figure 8, with the *X*-axis aligned in the direction of travel, and the origin taken to be when the measuring tap enters the crosswind generator, indicated by a series of light sources and the on-board light detector. The *Y*-axis is the horizontal plane perpendicular to the track direction, measured from the centre of track and the *Z*-axis is in the vertical direction measured from the top of the rail.

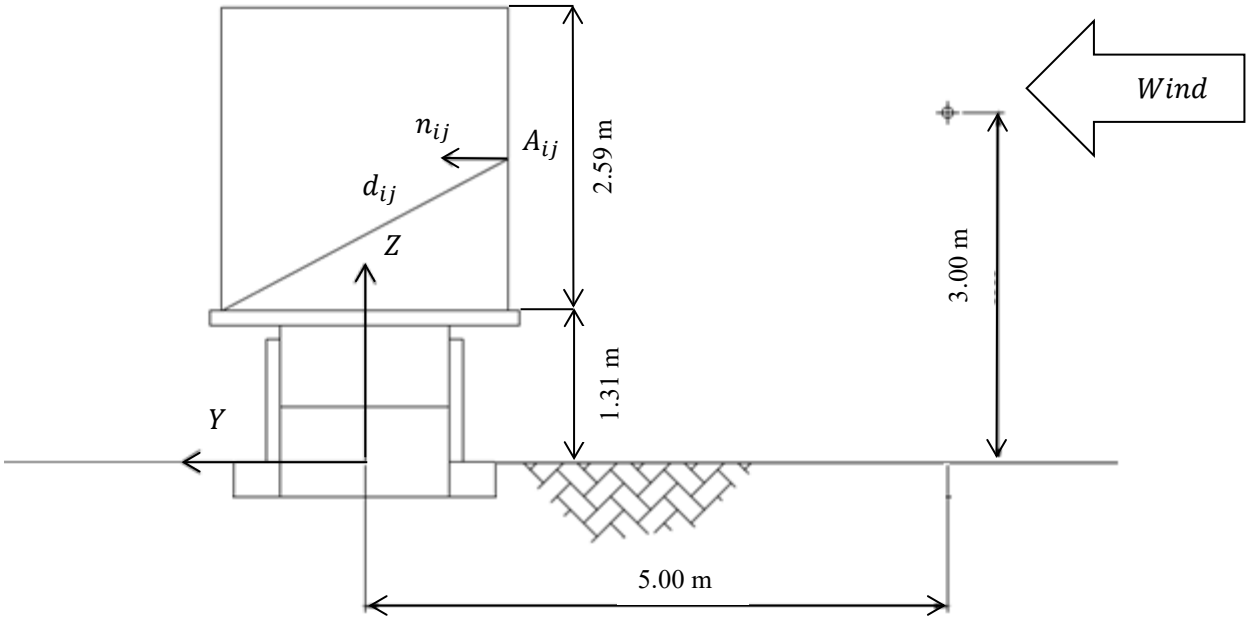

Figure 8: The coordinate system defined for the crosswind experiments at the TRAIN rig. The direction of train travel is in the X-direction out of the page. The Cobra probe reference position is also shown in relation to the model in the crosswind test section. The index ij is used to identify pressure taps such that j is the tapping loop and i is the associated tap on that loop (figure 7). All dimensions are given as the relative full-scale measurements.

Localised crosswind velocity and static pressure measurements were made using Series 100 Cobra probes (TFI, 2011). The probe was used to carry out a flow characterisation of the crosswind generator, as well as a method of monitoring crosswind conditions in the main experiments at a specified reference position; 4.78 m from the crosswind generator train entrance portal at a distance of 0.2 m upstream of the tracks, measured at the reference height of $Z_{ref} = 0.12$ m. The reference position, also used in the crosswind flow characterisation as spanwise position 16 (figure 3), provides a comparison from which to extrapolate out run to run variation in flow speed and static pressure

(Soper, 2014). Flow properties were recorded for 240 seconds at a sampling frequency of 2000 Hz to ensure the spectral content of the simulated wind could be assessed.

Model speed was measured using a series of opposing SICK photoelectric position finders and reflectors set up along the trackside. Train speed was calculated based on the time taken for the model to break both beams, to an accuracy of ±0.1 m/s. A series of light sources were positioned close to the entrance and exit of the crosswind generator. As the train passed a light source the on-board light detector would measure a change in voltage, which was used to assist in aligning data. Ambient conditions were monitored using an Oregon Scientific BAR208HGA weather station to measure room temperature (±1˚C) and relative humidity (±1%) and a GBP3300 Digital Barometer to measure atmospheric pressure (±1 mb/100 Pa). Air density ρ was calculated using the gas constant R = 287 (J/kg K) and the room temperature.

2.4 Data analysis methodology

The surface pressure distribution is presented in terms of a series of non-dimensionalised pressure coefficients, derived from time averaging the coefficient time history. As discussed, the flow characterisation exhibits limited spanwise uniformity in $\overline{u_{cwg}}$, with variations in turbulence intensities relating to amplifications associated with $\overline{u_{cwg}}$, the relative position in relation to fans and the confined nature of the crosswind system within the building envelope. A quasi-steady method was developed for calculating time average pressure coefficients at a series of spanwise positions (S_N); taking into account a spanwise varying reference wind velocity and the decrease in train speed (ΔV_{train}) across the crosswind generator. Figure 9 illustrates the effect of variations on the magnitude of relative mean wind velocity V_{rel}.

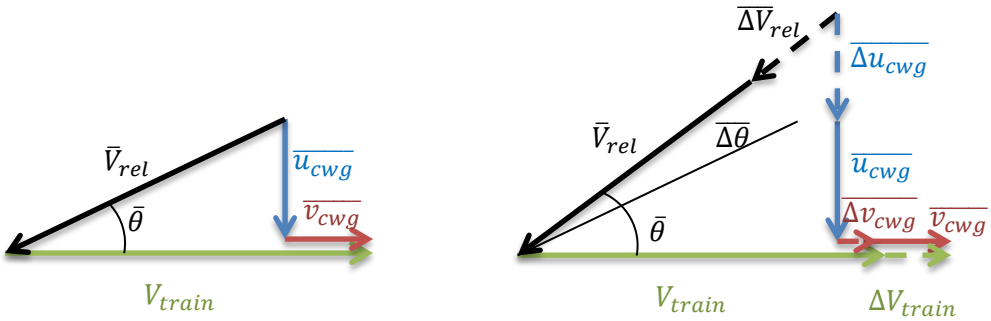

a) Nominal reference velocity b) Relative reference velocity

Figure 9: A vector diagram to show mean wind velocity relative to a moving vehicle for a) a nominal mean wind b) relative mean wind fluctuations.

By taking spanwise variations in mean relative crosswind velocities into account, the surface pressure coefficient time histories for individual runs (r) are calculated for a series of spanwise positions (S_N), rather than a total spanwise average:

$$C_{P_{ij}}(t, S_N, \theta) = \frac{P_{ij}(t) - \bar{P}_{ST}(S_N, \theta)}{\frac{1}{2}\rho\left(\bar{V}^*_{rel}(S_N)\right)^2} \quad (1)$$

where $N = 64$, as defined in the flow characterisation and the relative wind velocity $\bar{V}^*_{rel}$ is given by,

$$\bar{V}^*_{rel}(S_N) = \sqrt{\left[\bar{u}^*_{cwg\ SW}(S_N)\right]^2 + \left[V_{train,SW}(S_N) - \bar{v}^*_{cwg\ SW}(S_N)\right]^2} \quad (2)$$

The index ij is used to identify pressure taps such that j is the tapping loop and i is the associated tap on that loop (figure 7). $P_{ij}(t)$ is the instantaneous surface pressure at tap ij at time t, in respect to the reference pressure measured from the sealed container on the train and $\bar{P}_{ST}(S_N, \theta)$ is the wind mean static pressure associated to spanwise position S_N and yaw angle θ, in respect to the atmospheric pressure. Pressure measurements made before the train was in motion (atmospheric pressure with a reference to the sealed on-board container) enabled a transformation to be made to equation 1 (see Soper (2014) for a full derivation). The over bar notation denotes a time average and the subscript SW denotes a spanwise average over the portion of crosswind test section $\left(L_{CW_{S_N}}\right)$ associated with spanwise position (defined as extending half way to neighbouring S_N or the crosswind test section edge). The $*$ superscript denotes when a crosswind variable has been corrected to account for streamwise gradients assessed within the crosswind flow characterisation (Dorigatti, 2013).

Time histories are essentially deconstructed into a series of time histories for each spanwise position, with an associated yaw angle θ_{r,S_N}. Ensemble time averages are created by refinement of mean

pressure coefficients to only accepting instantaneous values of C_p within the range $\theta_{r,S_N} = 30° \pm 2°$, thus creating an ensemble time average coefficient of pressure $C_{p_{ij}}$ with respect to an ensemble mean yaw angle $28^\circ \leq \bar{\theta}_{ENS} \leq 32^\circ$ at positions S_N (Cooper, 1993; Dorigatti, 2013),

$$\overline{C_{P_{ij}}} = \overline{C_{P_{ij}}(S_N, \bar{\theta}_{ENS})|_{ENS}}|_{\bar{\theta}_{ENS} \in 30° \pm 2°} \quad (3)$$

In general, 15 repeats were carried out for each tapping setup to create ensemble averages in line with TSI specifications and ensemble stability experiments (TSI, 2008; Soper, 2014). In relation to pressure coefficient results calculated using a spanwise average across the whole crosswind generator, Dorigatti (2013) observed that the greatest differences occurred in areas with a large suction magnitude associated with flow separation/recirculation. Pressure coefficient time histories calculated using the spanwise varying method exhibited a smoothing effect, indicating a reduced effect from the spanwise inhomogeneity of the crosswind flow.

The non-dimensionalised aerodynamic coefficients for side and lift forces and the rolling moment were measured in a reference system about the leeward container base edge, as shown in figure 8. The aerodynamic load coefficients are examined using average surface pressure coefficient data through a method developed by Sanquer et al. (2004); Quinn et al. (2007) and Dorigatti et al., (2014). The relative non-dimensional force coefficients are estimated through integrating surface pressure coefficients on a discretised geometry of a vehicle surface. Discretised areas are formed by creating a rectangle centred on each tapping point, extending halfway to neighbouring tapping points or to container edges for outer tapping points (figure 7). The overall load coefficients can be defined as (Quinn et al., 2007; Dorigatti et al., 2014),

$$C_Y = \frac{F_Y}{\frac{1}{2}\rho V_{rel}^2 A_{ref}} = \frac{\sum_i \overline{C_{P_{ij}}} A_{ij} (\boldsymbol{n}_{ij} \cdot \boldsymbol{y})}{A_{ref}} \quad (4)$$

$$C_Z = \frac{F_Z}{\frac{1}{2}\rho V_{rel}^2 A_{ref}} = \frac{\sum_i \overline{C_{P_{ij}}} A_{ij} (\boldsymbol{n}_{ij} \cdot \boldsymbol{z})}{A_{ref}} \quad (5)$$

$$C_{M_{X,lee}} = \frac{M_{X,lee}}{\frac{1}{2}\rho V_{rel}^2 A_{ref} H_{ref}} = \frac{\sum_i \overline{C_{P_{ij}}} A_{ij}}{A_{ref} H_{ref}} \frac{\|\boldsymbol{d}_{ij} \times \boldsymbol{n}_{ij}\|}{\boldsymbol{x}} \quad (6)$$

where F_Y and F_Z are side and lift forces respectively and $M_{X,lee}$ is the rolling moment force. $\overline{C_{P_{ij}}}$ is the ensemble average pressure coefficient for each pressure tapping associated with discretised area A_{ij}. V_{rel}, A_{ref} and H_{ref} are reference values for relative velocity, the side area of the measuring container and the height of the measuring container, respectively. For this study A_{ref} and H_{ref} are defined for the measuring container to assess the influence of container loading configuration and the crosswind effect on a loaded container. Therefore, H_{ref} is the nominal container height 2.59 m and A_{ref} is the nominal side area of the container, which for partially loaded consists is 31.58 m^2 and for the fully loaded consist is 47.37 m^2. $\boldsymbol{n}_{ij}$ are normal unit vectors associated with discretised areas A_{ij}, and $\boldsymbol{d}_{ij}$ are the vectors perpendicular to the container base leeward edge, directed from each pressure tap.

2.5 Uncertainty analysis

An uncertainty analysis methodology, developed by Taylor (1997) and Tavoularis (2005), is applied to mean pressure and aerodynamic load coefficients.

Throughout this study experimental data is presented in terms of non-dimensional coefficients. These coefficients are calculated using a series of measured variables. To account for the combined influence of individual uncertainties associated with each variable, the theory of propagation of error is applied to calculate the coefficient uncertainty (Taylor, 1997). Total uncertainty E_{TOT} is defined as the sum of random uncertainties and the uncertainty of a measured variable due to instrumentation accuracy. To account for the random variability relating to the run to run unsteadiness of the physical phenomenon measured, the random uncertainty is defined as assuming a normal distribution and considering a confidence level of 95%. The uncertainty of a measured variable is quantified by assessing the characteristics and performance limits of the experiment instrumentation. Taylor (1997) states that according to the propagation of error, the uncertainty of a measured variable is defined as,

$$E_{BIAS} = \sqrt{\sum_k \left(\frac{\partial C_P}{\partial b_k}\delta b_k\right)^2} \quad (7)$$

where C_P is the non-dimensional pressure coefficient and the subscript k relates to individual pressure transducers installed in the on-board data logger. b_k indicates an individual quantity measured for the calculation of C_P, and ∂b_k represents the uncertainty associated with the measuring instrumentation. Instrumentation uncertainty is caused by hysteresis and non-linearity, and is usually supplied in manufacturer specifications and considered to be a uniform distribution of uncertainty across the instrument range. For the differential pressure transducers the instrumentation uncertainty is non-linear and calculated as the maximum error from an instrumentation calibration using a Betz micro manometer (Acin, 2014).

The uncertainties associated with the mean aerodynamic load coefficients are estimated relative to the uncertainties calculated for the mean pressure coefficients. Applying propagation theory to the aerodynamic load coefficient equations (equations 4-6), and assuming the load calculated for the discretised area associated to each pressure tap are independent, the uncertainty of the mean aerodynamic load coefficients can be defined as:

$$E_{LOAD} = \sqrt{\sum_i \left(\sum_j \left(\frac{\partial C_\xi}{\partial C_{P_{ij}}} E_{TOT_{ij}} \right) \right)^2} \quad (8)$$

where ξ relates to the different non-dimensional quantities calculated, i.e. C_Y, C_Z and $C_{M_{X,lee}}$.

	Consist number		
	1	2	3
C_Y	0.016	0.022	0.022
C_Z	0.018	0.029	0.028
$C_{M_{X,lee}}$	0.016	0.026	0.025

Table 2: Mean total uncertainties for aerodynamic load coefficients C_Y, C_Z and $C_{M_{X,lee}}$ for consists 1, 2 and 3.

The values in table 2 provide an estimate of the uncertainties of each aerodynamic load coefficient. The uncertainties are considered to be conservative estimations to the true error, as the calculation does not account for the uncertainty introduced through discretising the container geometry and by the

assumption of pressure uniformity across each discretised area in the pressure integration process (Dorigatti, 2013). The uncertainty process was repeated for two further container discretisation methods and minimal differences observed between each.

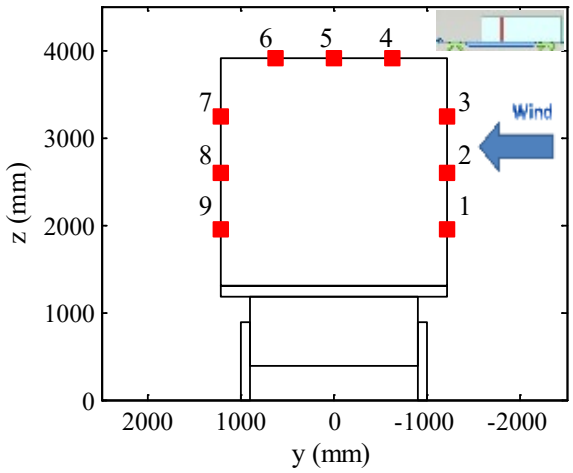

a) Loop 2 pressure tap layout

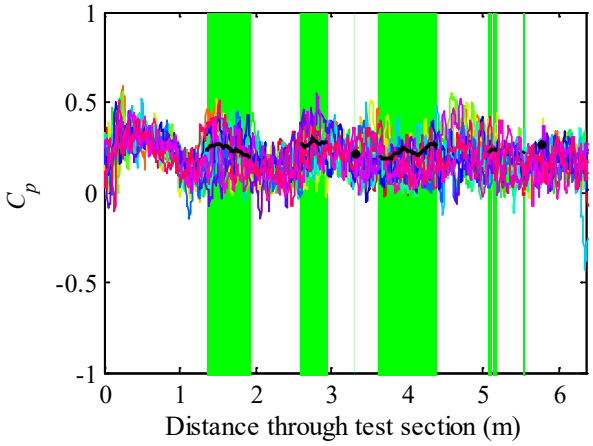

b) Loop 2 tap 2

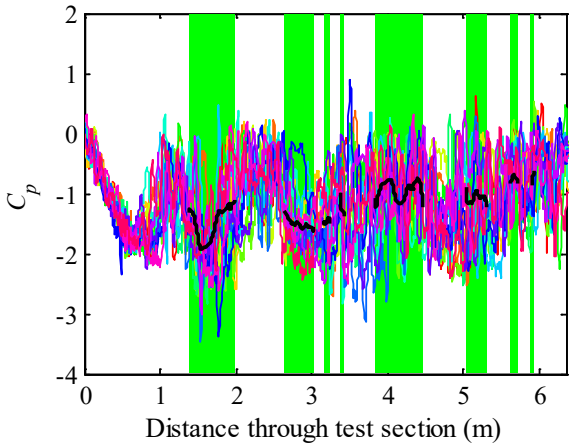

c) Loop 2 tap 4

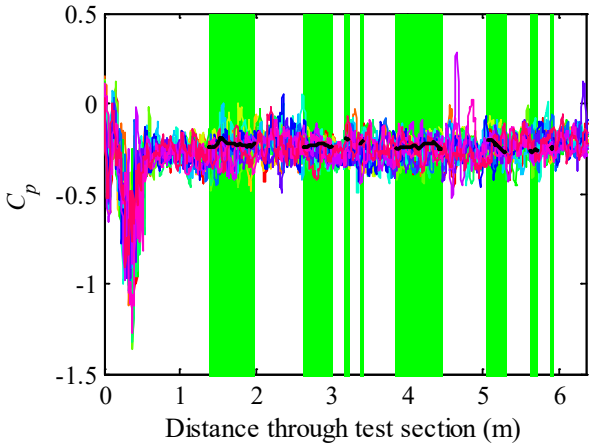

d) Loop 2 tap 5

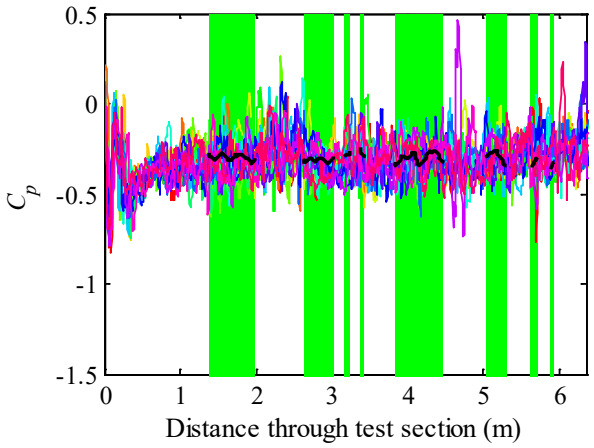

e) Loop 2 tap 6

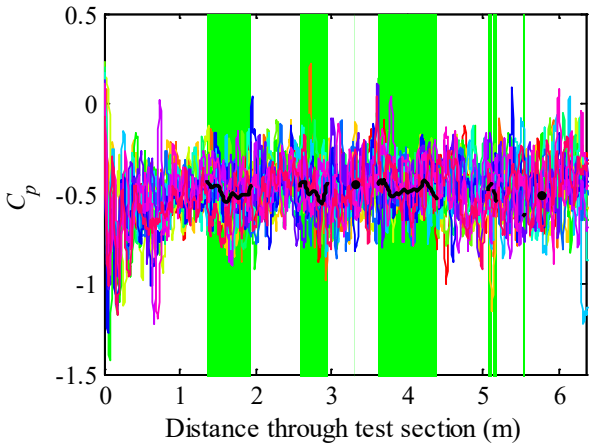

f) Loop 2 tap 8

Figure 10: Examples of the typical evolution of pressure coefficient as the train travels within the crosswind generator. A series of 15 individual runs are plotted with the corresponding deconstructed ensemble average time series for consist 3. Areas highlighted green are where the ensemble yaw angle $28° \leq \overline{\boldsymbol{\theta}}_{\boldsymbol{ENS}} \leq 32°$, dependent on the tapping setup.

3. Results and analysis

3.1 Pressure coefficient

Individual pressure coefficient time histories were analysed with respect to the corresponding deconstructed ensemble average. Figure 10 gives an example pressure coefficient time history, with areas highlighted in green corresponding to the deconstructed ensemble mean, such that yaw angle $28° \leq \bar{\theta}_{ENS} \leq 32°$. Variations in pressure coefficient at both ends of time histories are created by the vehicle transition when entering and exiting the crosswind test section. Figure 10 is representative of all pressure taps monitored on the measuring container for all consists tested. In general, good consistency is observed for the pressure coefficient evolution within the central bounds of the crosswind test section (20% to 90% of crosswind generator length) and even for results outside the ensemble mean yaw angle $28° \leq \bar{\theta}_{ENS} \leq 32°$ bounds. Each individual run exhibits a series of random high frequency fluctuations, of similar amplitude about the ensemble time series, created by the turbulent nature of the flow developing around the train when subjected to the crosswind. Larger fluctuation amplitudes are observed in combination with areas of the lowest values of pressure coefficient, associated with vortices attached to the train surface, or of regions of recirculation characterised by an increased level of turbulence. These areas are located close to container edges, expected to be the source of large flow separations.

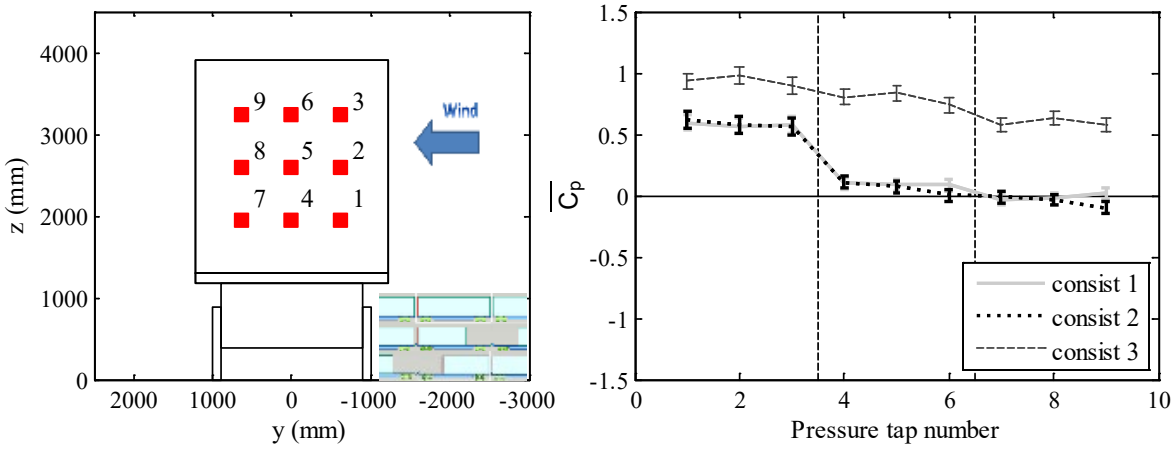

a) Loop 1 pressure tap layout

b) Loop 1 pressure coefficient

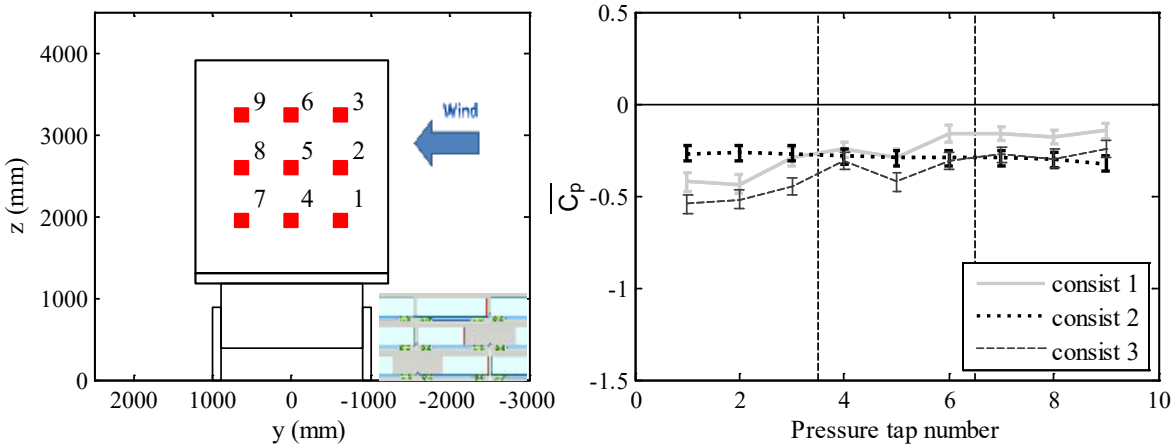

c) Loop 7 pressure tap layout

d) Loop 7 pressure coefficient

Figure 11: Mean surface pressure coefficient distribution with associated uncertainty error bounds for consists 1, 2 and 3 for loops 1 and 7. For each loop a diagram of the pressure tapping positions, shown as a series of red dots corresponding to each pressure tap, is provided.

In figures 11-13 the mean pressure coefficient distribution for each measuring loop are presented as a series of container cross sections for all consists. In each plot the wagon cross section illustrates pressure tap positions on the container surface and the crosswind direction. Bounds to the associated uncertainty for each pressure transducer are also plotted in accordance to which pressure tap the transducer was connected. Values of positive pressure coefficient indicate areas of stagnation, whereas, values of negative pressure coefficient are representative of areas of suction. In general, results exhibit similar magnitudes to previous passenger studies (Baker and Sterling, 2009, Dorigatti et al., 2014). However, areas associated with large flow separation exhibit greater magnitudes of pressure coefficient than previously observed in passenger studies.

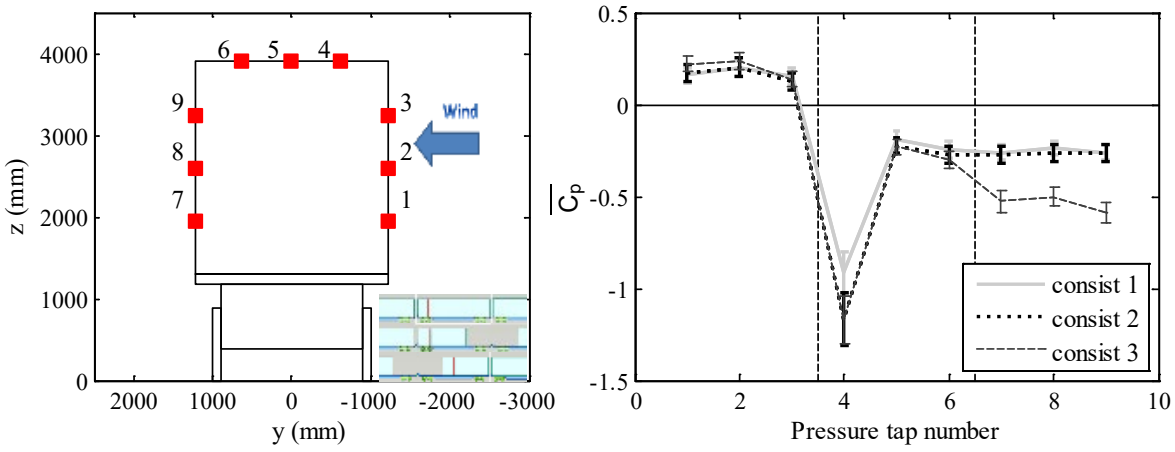

a) Loop 2 pressure tap layout

b) Loop 2 pressure coefficient

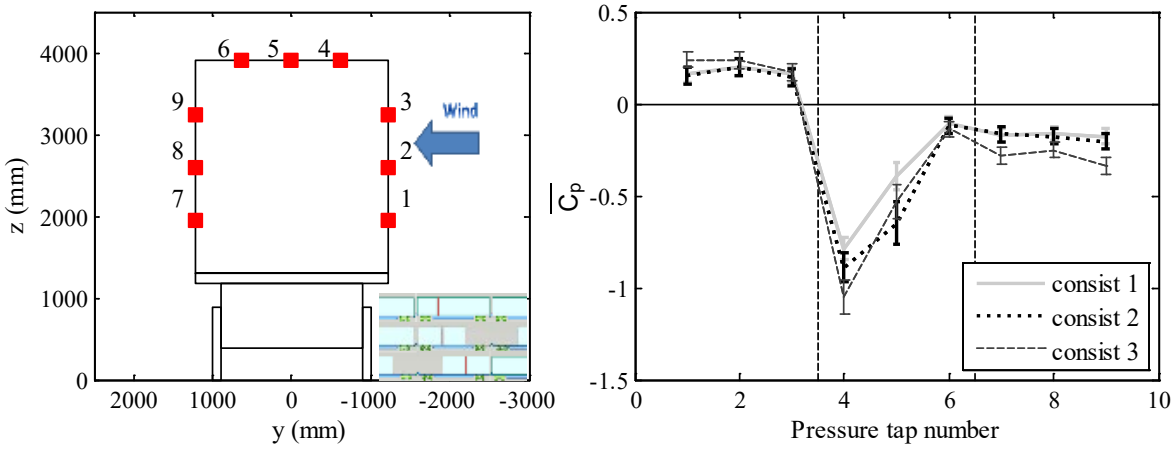

c) Loop 3 pressure tap layout

d) Loop 3 pressure coefficient

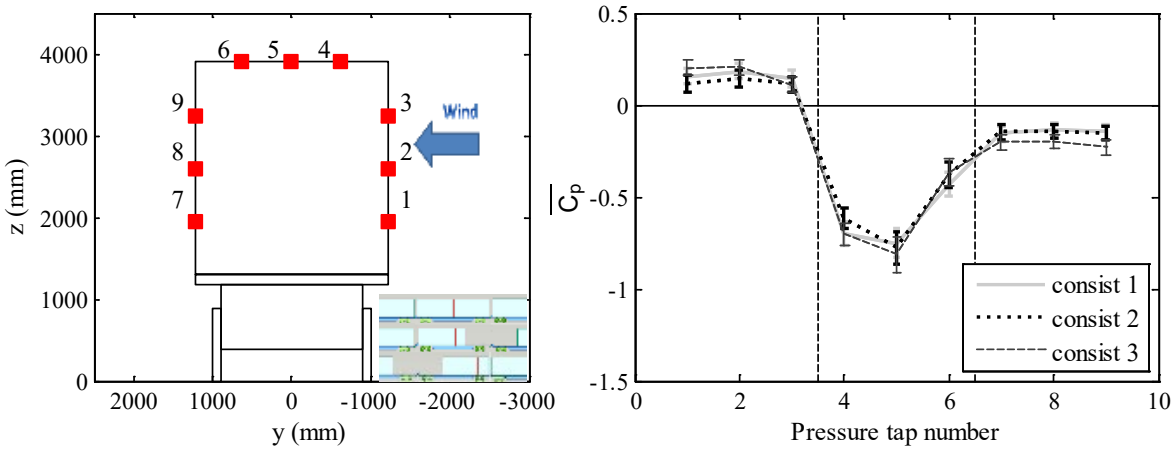

e) Loop 4 pressure tap layout

f) Loop 4 pressure coefficient

Figure 12: Mean surface pressure coefficient distribution with associated uncertainty error bounds for consists 1, 2 and 3 for loops 2, 3 and 4. For each loop a diagram of the pressure tapping positions, shown as a series of red dots corresponding to each pressure tap, is provided.

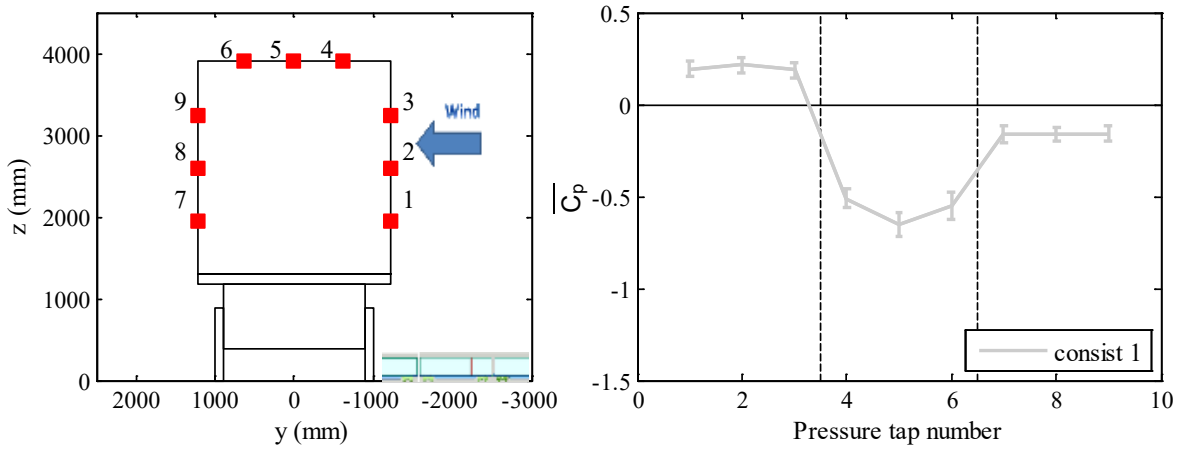

a) Loop 5 pressure tap layout

b) Loop 5 pressure coefficient

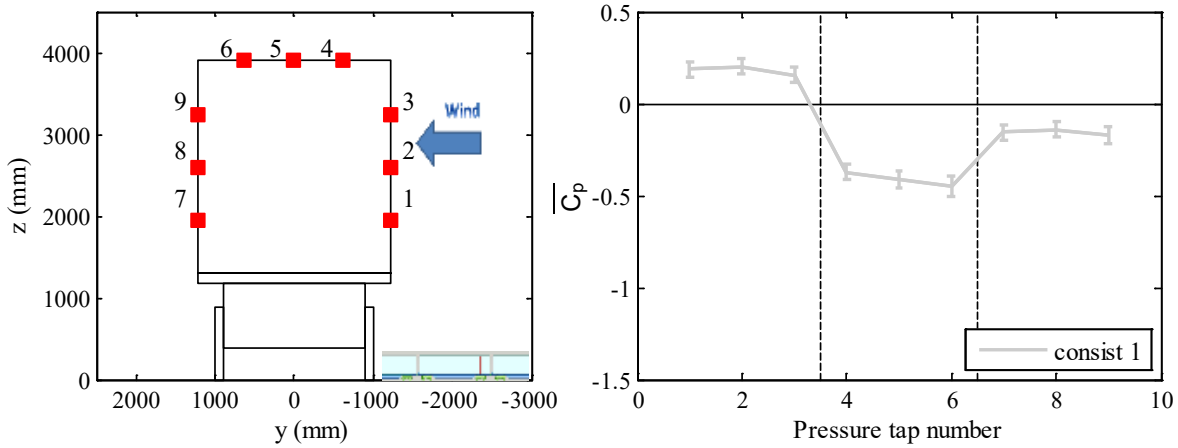

c) Loop 6 pressure tap layout

d) Loop 6 pressure coefficient

Figure 13: Mean surface pressure coefficient distribution with associated uncertainty error bounds for consist 1 for loops 5 and 6. For each loop a diagram of the pressure tapping positions, shown as a series of red dots corresponding to each pressure tap, is provided.

A series of flow patterns can be identified developing along the container length with variations noticeable for the different consists examined, exhibiting a dependence on container loading configuration. For example, the large space between the container loaded on the second wagon and the measuring container on the third wagon in consist 3 creates a region of stagnation with positive pressure on the lead face, with the largest magnitudes of pressure coefficient exhibited for pressure taps closest to the windward edge (figure 11b). The space between the container loaded onto the second wagon and the measuring container for consists 1 and 2 is much smaller than for consist 3; however, similarly to consist 3, the largest magnitudes of pressure coefficient are measured for pressure taps closest to the windward edge. In the centre of the lead face the pressure coefficient

magnitude is close to zero, and towards the leeward edge small magnitudes of negative pressure coefficient are observed. The container loaded onto the second wagon creates a shielding effect on the measuring container. As the space between these containers is much smaller for consists 1 and 2 the shielding effect is greater in relation to consist 3. The negative pressure coefficient measured towards the leeward edge suggests a suction of flow from the gap between loaded containers. As the freight train moves through the crosswind, flow is directed through the gap between loaded containers. A positive pressure is measured for pressure taps closest to the windward edge, associated with the impinging crosswind, creating an area of stagnation. Flow out from the space between containers creates a suction effect, as measured at the leeward edge.

Measurements at the rear face also suggest a movement of flow through the space between containers, dependent on loading configuration, shown in figure 11d). The rear face is characterised by an area of suction. Although the space size between containers in consists 1 and 3 is the same, there are clear differences in pressure distribution and magnitude across the rear face. At the windward edge there is greater negative pressure towards the base of the rear face, decreasing in magnitude towards to container roof. Moving across the rear face the greater negative pressure magnitude is seen to move up from the base pressure tap towards the middle pressure tap, with the pressure taps either side exhibiting a similar magnitude. It is suggested that flow is accelerated through the small gap between containers, with flow generally moving upwards in the gap. The impinging crosswind flow hits the lead face of the following container creating a positive pressure on the following container lead face and negative pressure on the measuring container rear face. Flow within the gap is drawn upwards and outwards by suction flow across the container roof and leeward face. This creates negative pressure on both the lead and rear faces towards the leeward side within the small gap. For consist 2 the large space following the measuring container negates the suction influence seen within the small gap, and thus a uniform pressure distribution is observed. The influence of container loading configuration is also observed between consists 1 and 3. For consist 3 the suction magnitudes at each pressure tap on the rear face are consistently 10% lower than for consist 1. Soper et al. (2014) highlighted the influence of container loading efficiency on boundary layer development, observing a series of pulse

peaks in boundary layer velocities created by large spaces before a loaded container. The influence of increased boundary layer velocities, due to loading configuration for consist 3, increases the magnitude of suction within the small gap between containers. This creates an overall greater magnitude for the negative pressure distribution on the rear face of consist 3 in comparison to consist 1.

The flow pattern on the windward face for all consists exhibits a relatively uniform area of stagnation with positive pressure. Small variations in pressure coefficient across the windward face lie within the associated error bounds for each tapping point. For consist 3 the influence of a large space before the measuring container creates a pulse peak increase to the boundary layer velocity around the measuring container. Higher slipstream velocities within the boundary layer combine with the onset wind velocity to create a larger relative crosswind magnitude, resulting in a larger pressure coefficient magnitude measured for consist 3 in comparison to consists 1 and 2.

The flow pattern across the roof, for all consists, is characteristic of a roll vortex spreading across the roof, emanating from the windward corner of the lead face (Castro and Robins, 1977; Hemida and Baker, 2010). The roll vortex is characterised by a large negative peak at the pressure tap closest to the windward edge for loop 2 and uniform magnitudes for other pressure taps on loop 2. The negative peak in pressure varies in intensity and position across the roof face, spreading towards the leeward edge as distance along the container from the lead face is increased. The flow separation creates unsteadiness in the pressure coefficient time history. The lateral spread of the roll vortex creates increased standard deviation values across the container roof, emanating from the windward corner. For consists 2 and 3 the flow pattern is visible close to the container rear, however for consist 1 relatively uniform pressure magnitudes and distribution are observed close to the container rear (figure 13). This suggests the roll vortex has moved towards the leeward roof edge and a possible detachment of the roll vortex from the container roof towards the rear of the measuring container has occurred for consist 1. For all consists the magnitude of the suction peak on the roof represents the lowest values of pressure coefficient on the container surface. The influence of container loading

configuration is also exhibited in the flow pattern across the roof. Pressure coefficient magnitudes across the roof for consist 3 are larger than for consists 1 and 2. The space before the measuring container in consist 3 negates any shielding effect for the windward corner at the lead face, from which the roll vortex forms. Similarly, although the measuring container is relatively shielded for consist 1 and 2, the decreased loading efficiency in consist 2 increases the magnitude of boundary layer development around the train, leading to an increased magnitude in the roll vortex in comparison to consist 1.

The flow pattern on the leeward face for all consists exhibits an area of suction with negative pressure. The pressure coefficients for consists 1 and 2 remain relatively uniform across the whole leeward face, except near the leeward lead face edge; suggesting complete detachment of vortices formed at the leeward lead face edge within a short distance of the edge. For consist 2 a small pressure gradient from the lead to rear face is observed. The pressure gradient is much smaller for consist 1, suggesting an influence from the container loading configuration on boundary layer development. Consist 3 exhibits the largest variation in pressure coefficient on the leeward face. Following the leeward lead face edge there is a large suction peak associated with a vortex emanating from the leeward edge of the lead face. Pressure magnitudes measured indicate a steep pressure gradient toward the container rear; suggesting complete detachment of leeward vortices by the container rear, with pressure coefficient magnitudes measured towards the rear similar to leeward pressures measured for consists 1 and 2. The flow pattern observed is characteristic of a surface mounted cube under the influence of a crosswind and has been observed in freight crosswind studies previously (Hemida and Baker, 2010). Hemida and Baker (2010) found a series of large vortices, emanating from container edges, become detached from the container surface and move downstream with the crosswind. The pressure gradients observed for the 30° yaw angle suggest vortices become detached and move away from the container surface, increasing in distance from the container surface as the distance from the container lead face is increased.

3.2 Aerodynamic load coefficients

The overall mean aerodynamic load coefficients are calculated as the discrete integral of forces acting on each pressure tap area, through the application of equations 4-6. Figure 14 and table 3 show estimated values calculated for aerodynamic load coefficients on the measuring container for consists 1, 2 and 3.

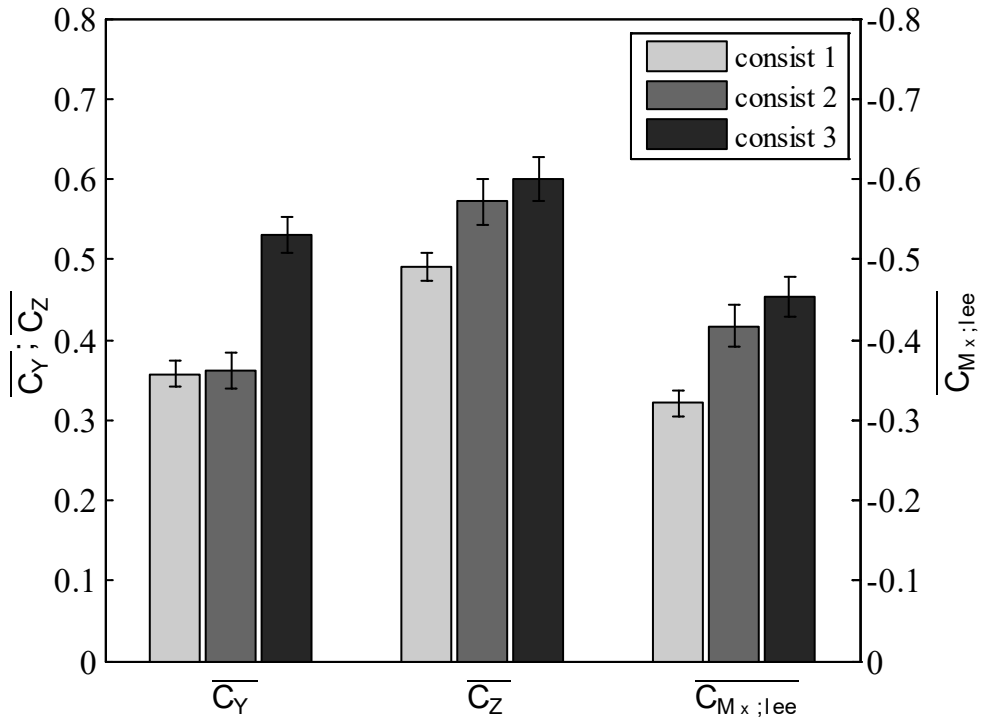

Figure 14: Estimated values for the aerodynamic load coefficients C_Y, C_Z and $C_{M_{X,lee}}$ in the crosswind test section. A conventional axis is adopted for C_Y, C_Z and an inverted axis for $C_{M_{X,lee}}$. The associated uncertainty bounds for each coefficient are also plotted.

	Consist number		
	1	2	3
C_Y	0.36	0.36	0.53
C_Z	0.49	0.57	0.60
$C_{M_{X,lee}}$	-0.32	-0.42	-0.45

Table 3: Aerodynamic load coefficients for consists 1, 2 and 3. Side and lift forces C_Y and C_Z, and the roll moment $C_{M_{X,lee}}$ are given with respect to a reference system about the measuring container.

Positive values for C_Y and C_Z indicate the overall lateral and vertical forces are directed with the crosswind flow and upward respectively. The roll moment is given in respect to the reference system about the leeward base container edge; ensuring negative values for moments $C_{M_{X,lee}}$ correspond to moments that overturn the vehicle. Results are characteristic of forces measured on a vehicle under the influence of a crosswind at a 30° yaw angle (Quinn et al., 2007; RSSB, 2012; Dorigatti et al., 2014).

Figure 14 illustrates clear differences in force and roll moment coefficients as container loading configuration varies. In general, larger magnitudes are observed as container loading efficiency is reduced. Although consists 2 and 3 have the same loading efficiency, the variation in loading pattern creates differences in force coefficients. Consist 3 has a large space before the measuring container in comparison to consist 2, which is relatively shielded by a container on the wagon in front. Forces acting on the measuring container in consist 3 have a greater influence from slipstream velocities within the boundary layer around the train. The container loaded on the wagon in front of has a shielding effect on the measuring container, reducing the magnitude of C_Y and C_Z for consists 1 and 2 in relation to consist 3, for which container leading edges are more susceptible to large flow separations. Values for C_Z and $C_{M_{X,lee}}$ for consist 2 are greater than for consist 1, however values of C_Y are similar. This suggests that the reduced container loading efficiency in consist 2 influences boundary layer development, which in turn increases the magnitude of the roll vortex created across the measuring container roof, as discussed in section 3.1. The difference in magnitude of C_Z between consist 1 and 2 accounts for the differences observed in $C_{M_{X,lee}}$.

Due to the method of container attachment the flatbed wagon was modelled as a solid loading base, thus no pressure taps were placed in the container base. If a spine loading system was adopted for the flatbed wagon, pressure taps would be needed in the container base to measure the flow underneath the wagon. It is hypothesised that as no structural changes occur to the flatbed wagon between loading configurations, the pressure coefficients measured on the container base would be similar for all

consists tested; thus, it is not expected that the exclusion of pressure taps from the container base would influence the general pattern of observed aerodynamic load coefficients. Dorigatti et al., (2014) observed negative pressure across the underbody of the Class 390 model, for both stationary and moving model experiments. Considering this in relation to the freight model, the value for C_Z would decrease in respect to the case with no underbody pressure coefficients considered.

Values for $C_{M_{X,lee}}$ exhibit an increasing magnitude as container loading efficiencies are reduced. In light of the 2008 UK crosswind incidents, RSSB (2012) carried out a series of wind tunnel experiments using a FEA type B flatbed wagon, loaded with a 12.19 m and 6.10 m container, and a HYA coal hopper wagon. At a yaw angle of 30° the estimated value for the roll moment is $C_{M_{X,lee}} = 0.78$ (RSSB, 2012). The exact setup within RSSB (2012) is not replicated in this study, however, by using values for $C_{M_{X,lee}}$ for consists 1, 2 and 3 it is possible to draw some comparisons. Considering the loading configuration tested in RSSB (2012), there is a large space in front and behind the measuring container. In comparison to consists 1, 2 and 3, the influence of a space in front and behind the measuring container increases the estimated value of $C_{M_{X,lee}}$, with the largest differences occurring for a space in front of the measuring container. Therefore, the values for consist 3 are considered to offer the closest comparison to the RSSB experiment setup. For consist 3 at a yaw angle of 30° the estimated value of $C_{M_{X,lee}} = 0.45$, exhibiting limited agreement. However, if the influence of an additional space behind the measuring container was considered, the value for $C_{M_{X,lee}}$ would increase, bringing the value of $C_{M_{X,lee}}$ closer to the value measured in RSSB (2012). Further comparisons with other studies could not be made due to differences in experimental setup and with the actual measurements made (Alam and Watkins, 2007a; Hemida and Baker, 2010).

4. Conclusions

For the first time, a detailed analysis of the influence of container loading configuration on crosswind effects on a freight train has been undertaken at model-scale. The results show a number of important findings,

1. It is possible to measure the surface pressure on a freight container loaded onto a flatbed wagon using an on-board data logger and pressure monitoring system. Results are compared with typical passenger train surface pressure coefficient magnitudes and similar values are observed for the freight container for a yaw angle of 30°. However, areas associated with large flow separation exhibit greater magnitudes than previously observed in passenger studies.
2. Relatively good consistency is observed for the pressure coefficient evolution through the crosswind test section, with a series of high frequency fluctuations created by the turbulent nature of the flow developing around the train.
3. Clear differences in surface pressure coefficients are observed for differing container loading configurations:
    a. The lead container face exhibits a region of stagnation, with magnitude dependent on container loading configuration. For all consists the largest magnitudes of pressure coefficient are measured closest to the windward edge, associated with the impinging crosswind. For consists 1 and 2 a pressure gradient across the lead face, from positive to negative pressure, suggests a suction of air from the gap between containers.
    b. The rear face is characterised by an area of suction, however, the distribution of pressure is dependent on the space size following the measuring container. For consist 2 the pressure distribution remains relatively uniform. Conversely, for consists 1 and 3 there is a large degree of variation in pressure distribution and magnitude across the rear face. Flow is accelerated through the small gap between containers, with flow generally moving upwards. Suction magnitudes for consist 3 are consistently 10% lower than for consist 1.

c. The flow across the container roof, for all consists, is characteristic of a roll vortex spreading across the roof, emanating from the windward corner of the lead face. Results for consist 1 suggest detachment of the roll vortex from the container roof towards the rear of the measuring container.

d. The flow pattern on the windward face, for all consists, shows a relatively uniform area of stagnation.

e. The flow pattern on the leeward face exhibits an area of suction. Pressure coefficients for consists 1 and 2 remain relatively uniform across the whole leeward face, except near the leeward lead face edge, suggesting complete detachment of leeward vortices. Consist 3 exhibits the largest variation in pressure coefficient, associated with detachment of vortices emanating from the leeward edge of the lead face. The pressure gradient observed for consist 3 suggests vortices become detached and move away from the container surface.

4. Larger magnitudes for aerodynamic load coefficients are observed as container loading efficiency is reduced and space size in front of the measuring container increased. For consists 1 and 2 the influence of a container loaded closely on the wagon in front has a shielding effect on the measuring container. For consist 3 the measuring container is unshielded thus magnitudes for C_Y and C_Z are higher due to large flow separations.
5. Comparison of $C_{M_{X,lee}}$ with a previous container freight wind tunnel study exhibited limited agreement.

Acknowledgements

The authors would like to thank Dr Sarah Jordan, Dr Francesco Dorigatti, and Martin Gallagher from the University of Birmingham, for their help with performing the moving model experiments. The work was financed by a University of Birmingham scholarship.

References

[1] RAIB. Detachment of containers from freight wagons near Cheddington and Hardendale 1st March 2008. Technical report, DfT Accident Investigation, 2009.

[2] ATSB. Rail Occurrence Investigation RO-2008-013. Technical report, ATSB Transport, 2008.

[3] Baker, C. J., A. Quinn, M. Sima, L. Hoefener, and R. Licciardello, Full-scale measurement and analysis of train slipstreams and wakes: Part 1 ensemble averages. *Proceedings of the Institution of Mechanical Engineers, Part F: Journal of Rail and Rapid Transit*, 1–17, 2013.

[4] Department for Transport DfT. Delivering a sustainable railway. *In:* TRANSPORT, D. F. (ed.), 2007.

[5] Woodburn, A., An investigation of container train service provision and load factors in Great Britain. *European Journal of Transport and Infrastructure Research Volume 11* (3), 147–165, 2008.

[6] Soper, D., C. J. Baker, M. Sterling. Experimental investigation of the slipstream development around a container freight train using a moving model facility. *Journal of Wind Engineering and Industrial Aerodynamics Volume 135,* 105-117, 2014.

[7] Dorigatti, F. *Rail vehicles in crosswinds: analysis of steady and unsteady aerodynamic effects through static and moving model tests*. Ph.D. thesis, University of Birmingham, 2013.

[8] Dorigatti, F., M. Sterling, A.D. Quinn and C.J. Baker. Crosswind effects on a model passenger train - a comparison of static and moving experiments. *Journal of Wind Engineering and Industrial Aerodynamics Volume 138,* 36-51, 2015.

[9] Gawthorpe, R. Wind effects on ground transportation. *Journal of Wind Engineering and Industrial Aerodynamics Volume 52*, 73–92, 1994.

[10] RSSB. Resistance of Railway Vehicles to Roll-Over in Gales, Railway Group Standard GM/RT 2142. Technical report, Rail Safety and Standards Board Limited, London, 2009.

[11] Andersson, E., J. H¨aggstr¨om, M. Sima, and S. Stichel. Assessment of train overturning risk due to strong cross-winds. *Proceedings of the Institution of Mechanical Engineers, Part F: Journal of Rail and Rapid Transit Volume 218* (3), 213–223, 2004.

[12] Alam, F. and S. Watkins. Effects of crosswinds on double stacked container wagons. *16th Australasian Fluid Mechanics Conference*, December 3-7, Gold Coast, Australia, 2007a.

[13] Alam, F. and S. Watkins. Lateral stability of double stacked container wagon under crosswinds. In *Proceedings of the International Conference on Mechanical engineering (ICME2007), Dhaka, Bangladesh,* 2007b.

[14] Baker, C. and M. Sterling. Aerodynamic forces on multiple unit trains in crosswinds. *Journal of Fluids Engineering Volume 131*, 101–103, 2009.

[15] Raghunathan, R. S., H.-D. Kim, and T. Setoguchi. Aerodynamics of high-speed railway train. *Progress in Aerospace sciences Volume 38* (6), 469–514, 2002.

[16] Technical Specifications for Interoperability. Commission decision of 21 February 2008 concerning the technical specification for interoperability relating to the rolling stock subsystem of the trans-european high-speed rail system. Technical report, Official Journal of the European Union, 2008.

[17] Hemida, H. and C. Baker. Large-eddy simulation of the flow around a freight wagon subjected to a crosswind. *Computers & Fluids Volume 39, Issue 10*, 1944–1956, 2010.

[18] RSSB. Investigation of freight vehicle aerodynamic performance in accordance with GM/RT 2142 Resistance of Railway Vehicles to Roll-over in Gales. Technical report, Rail Safety and Standards Board Limited, London, 2012.

[19] Soper, D. *The aerodynamics of a container freight train*. Ph.D. thesis, University of Birmingham, 2014.

[20] Baker, C.J., S.J. Dalley, T. Johnson, A.D. Quinn, N.G. Wright. The slipstream and wake of a high speed train, *Proceedings of the Institution of Mechanical Engineers F Journal of Rail and Rapid Transit,* 215, 83-99, 2001.

[21] Baker, C.J., S. Jordan, T. Gilbert, A.D. Quinn, M. Sterling, T. Johnson, and J. Lane. "Transient aerodynamic pressures and forces on trackside and overhead structures due to passing trains. Part 1: Model-scale experiments; Part 2: Standards applications." *Proceedings of the Institution of Mechanical Engineers, Part F: Journal of Rail and Rapid Transit* 228, no. 1: 37-70, 2014.

[22] Ziehl-Abegg. Axial Fans Series FC. Available at http://www.ziehl-abegg.com. Last accessed 30/09/2014.

[23] TFI, Turbulent flow instrumentation - Cobra Probe - Getting started guide, 2011.

[24] Sensortechnics. HCLA Series miniature amplified low pressure sensors. Available at www.sensortechnics.com. Last accessed on 30/09/2014.

[25] Saunders, J., S. Watkins, and R. Cassar. Vortex optimisation of slotted tops and cavities of two different open rail wagons. *Journal of Wind Engineering and Industrial Aerodynamics.* Volume 49 (1-3), 421-430, 1993.

[26] Cooper, K. Bluff body aerodynamics as applied to vehicles. *Journal of Wind Engineering and Industrial Aerodynamics.* Volume 49 (1-3), 1-21, 1993.

[27] Sanquer, S., C. Barre, M. D. de Virel, and L.-M. Cleon. Effect of cross winds on high-speed trains: development of a new experimental methodology. *Journal of Wind Engineering and Industrial Aerodynamics Volume 92* (7), 535–545, 2004.

[28] Quinn, A., M. Sterling, A. Robertson, and C. Baker. An investigation of the wind-induced rolling moment on a commercial vehicle in the atmospheric boundary layer. *Proceedings of the Institution of Mechanical Engineers, Part D: Journal of Automobile Engineering Volume 221* (11), 1367–1379, 2007.

[29] Taylor, J. R. *An introduction to error analysis: the study of uncertainties in physical measurements*. University science books, 1997.

[30] Tavoularis, S. *Measurement in fluid mechanics*. Cambridge University Press, 2005.

[31] Acin. Betz micro-manometer – Factory standard for pressure calibration. Available at http://www.acin.nl. Last accessed on 24/09/14.

[32] Castro, I. and A. Robins. The flow around a surface-mounted cube in uniform and turbulent streams. *Journal of Fluid Mechanics Volume 79* (02), 307–335, 1977.